Ray-Tracing Based Image Correction of Optical Distortion for PIV Measurements in Packed Beds

Fabio J. W. A. Martins,[a,*] **Clauson Carvalho da Silva,**[b] **Christian Lessig,**[b] **Katharina Zähringer,**[a]

[a]Laboratory of Fluid Dynamics and Technical Flows (ISUT), Otto-von-Guericke-Universität Magdeburg, Universitätsplatz 2, D-39106 Magdeburg, Germany

[b]Institute for Simulation and Graphics, Otto-von-Guericke-Universität Magdeburg, Germany

Abstract. Packed beds are employed in a wide range of industrial processes, making their optimization an important objective. This requires a thorough understanding of the flow characteristics in the interstices of the bed and the influence of parameters such as packing material, fluid type and flow rate. Next to numerical simulations that have been performed, liquid flows in packed beds have been experimentally investigated by Particle Image Velocimetry (PIV), with optical accessibility obtained using refractive index matching and transparent geometries. For gaseous flows through packed beds, where refractive index matching is not available, there is, in contrast, still a lack of experimental work, because the different optical properties of gas and transparent packing geometries generate optical aberrations. The approximation of gaseous flows with results from dynamically similar, liquid flows provide thereby no reliable alternative because they might be inaccurate and lead to incorrect conclusions about the actual gas flow. The high optical aberrations created by transparent packed beds in PIV experiments can be corrected using ray tracing simulations of a geometric-optical model of the viewing media. The present work proposes a novel image correction technique based on this approach that overcomes the considerable optical distortions caused by arrangements of transparent solid spheres. We analyze the influence of spheres along the camera view in three test cases: the first studies optical distortions of target images, the second PIV computations of a known displacement of a printed particle field, and the third PIV measurements of an air-jet flow. The image correction is qualitatively and quantitatively evaluated by computing errors in target images and in velocity fields. We show that the high optical aberrations that are caused by the spheres can mostly be corrected using ray tracing, allowing for accurate optical measurements in complex geometries, such as packed beds. The approach proposed in this work might be extended to even more challenging geometries in order to solve limitations of existing techniques in the literature.

Keywords: Ray tracing, PIV, image correction, image pre-processing, optical distortions, spheres, packed bed.

* Correspondence Author**,** E-mail: fabio.martins@ovgu.de

1   Introduction

Packed beds are employed in a myriad of industrial processes, such as stripping, heat transfer, absorption, distillation and catalysis. They generally consist of a chamber filled with a granular packing material with a fluid flowing through the interstices. The flow characteristics inside the interstitial spaces, which depend, among other things, on the packing material, the type of fluid and its flow rate, greatly influence the performance of the packed bed. Motivated by this, the present work proposes an extended Particle Image Velocimetry (PIV) technique to accurately measure flow fields inside the interstices of packed beds.

In recent years, increasing efforts have been made to characterize the flow dynamics inside packed beds using either computational simulations[1-4] or experiments. Optical techniques such as Particle Tracking Velocimetry (PTV) and Particle Image Velocimetry (PIV)[5] are able to measure

the flow inside the interstices of packed beds experimentally. Because of complex geometries and setup constraints, most of these studies applied refractive index matching (RIM)[6-8] of liquid flows inside transparent models. RIM eliminates the refraction that arises when light rays pass between materials with different refractive indices, providing direct optical accessibility. PTV and PIV along with RIM have been successfully employed by many researchers to study packed beds and porous media.[9-14]

An alternative approach to avoid optical distortions is to use endoscopic PIV (EPIV).[15,16] The technique allows for optical access and light sheet delivery by compact probes. Blois and coworkers employed EPIV to analyze velocity fields and coherent structures of water flows inside the pore space of a packed bed overlain by a free-surface flow.[17]

Despite these efforts, there is currently still a lack of experiments investigating gaseous flows through packed beds. This is mainly due to the unavailability of refractive index matching in this setting and the lack of robust methods to correct for the optical distortions that are therefore unavoidable. Currently, often similarity analyses based on results obtained for dynamically similar, liquid flows are employed. However, without experimental reference values the reliability of this approach is unclear.

First efforts to overcome the optical distortion use the pinhole[18,19] and polynomial models[20,21]. Prasad and Adrian employed geometrical optics using ray tracing in a twin-camera stereo PIV.[18] The basic pinhole calibration model adopted by these authors provided all intrinsic and extrinsic camera parameters (i.e., focal length, magnification factor, camera position and orientation of image plane with respect to the object). However, it is not suitable in the presence of distortions caused by imperfect imaging optics. In such cases, polynomial calibration models are more appropriate due to their robustness and easier implementation. For example, Soloff and coworkers proposed a generalized, least-square polynomial with cubic dependence in the in-plane components but quadratic dependence in the out-of-plane component to correct optical distortions in stereo PIV.[20] Willert proposed a similar approach for PIV of wind tunnel flows using quadratic dependence in the in-plane components and linear dependence in the out-of-plane component.[21]

Kováts and coworkers were able to measure an air-flow velocity field not only in the interstices between hollow acrylic spheres of a coarse packed bed but also behind one-level of spheres.[22]

They accomplished this by locally adapting a polynomial calibration model to correct for the distortions. Nevertheless, the curvature of the hollow spheres precluded velocity measurements at the rim of the spheres and their accuracy was limited due to the low optical quality of the spheres they employed.

Polynomial algorithms fail in the presence of high optical distortions, as the ones that occur when imaging through complex transparent packed beds. In such cases, ray tracing together with geometrical and optical models of the viewing media can be employed to correct the image or the computed velocity field. Kang and coworkers implemented two PIV correction methods based on ray tracing to measure the flow field inside an evaporating droplet.[23] Later, Minor and coworkers re-derived Kang's correction algorithm to account for a more general situation with droplet shapes approaching a sphere.[24] Recently, Zha and coworkers proposed two methods, based on a mixture of ray tracing and polynomial fitting, to deal with the significant aberrations that are caused by the high curvature of the piston crown in a combustion engine.[25] However, most of the proposed image correction methods, as the aforementioned examples, assume axisymmetric geometry to correct for just moderate optical distortions.

A systematic correction of optical distortion is mandatory to obtain reliable quantitative measurements of the flow dynamics in packed beds. The present work proposes a novel image correction methodology that uses ray tracing to correct for the considerable optical aberration that is caused by transparent, solid spheres. We use ray tracing to determine the correspondence between points in the 3D scene and points on the image plane. This then allows us to invert the distortion and obtain an image close to that without the transparent spheres. We demonstrate accurate optical measurements of flow fields through complex geometries, such as packed beds, first for regular spherical arrangements, and ultimately for more challenging volumes.

2   Image corrections

The image correction method proposed in the present work uses ray tracing to compensate for the optical distortion resulting from imaging through clear-glass spheres. The procedure consists of creating a 3D model of the experimental setup and then using ray tracing to determine the correspondence between world coordinates in the 3D environment and pixel coordinates in the 2D image. Fig. 1 illustrates a 3D environment with one sphere with radius R (transparent blue sphere) and a camera positioned orthogonally to an investigation plane at $z = 0$ (grey grid), with

its center C at $z = 10R$. The camera center C refers to the so-called principal point, which is used as the origin of all light rays in the implementation. The camera sensor is represented by its virtual image plane at $z = 8.5R$ (black plane) in the viewing frustum. The pyramidal-shaped limits of the viewable region of the camera are plotted as thin blue lines. An exemplary light ray is plotted as magenta line and the principal ray, which is orthogonal to the camera sensor, as red line.
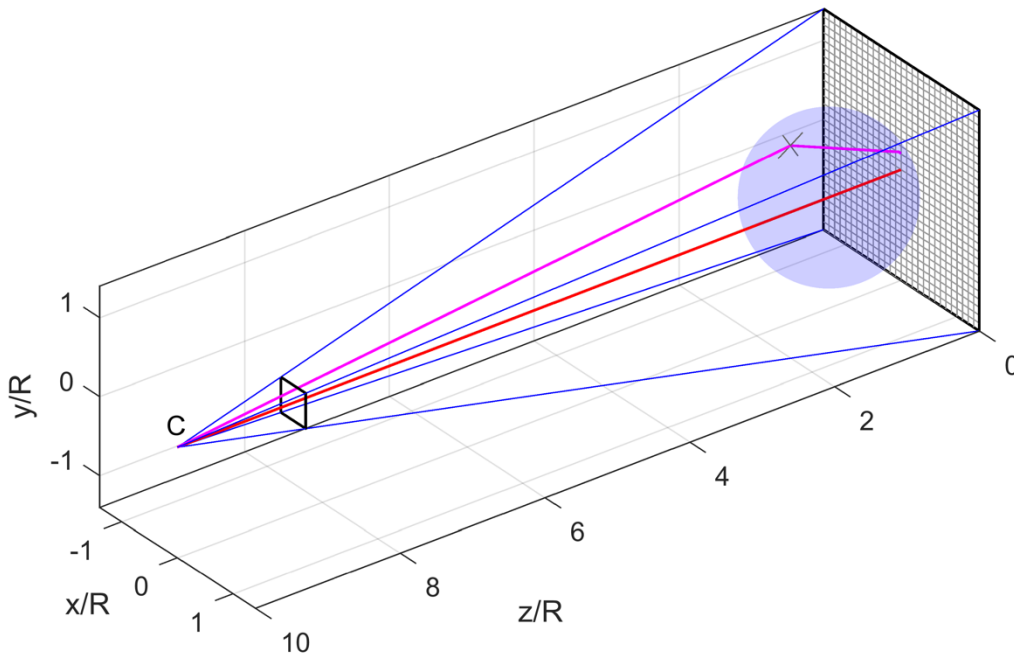
Fig. 1: 3D computational environment emulating the experimental setup with one transparent sphere to generate the ray-tracing mapping.

The open source software "pbrt" is employed for computing the correspondence between world coordinates on the investigation plane and pixel coordinates.[26] We employ a pinhole camera model due to its simplicity and since it provided sufficient accuracy even for the high aberrations that arise in the complex setups that will be presented in Section 4 ("pbrt" provides a more realistic camera model that might become necessary in future work).

The "pbrt" software simulates light propagation and scattering in a 3D environment and it can account for multiple, perfectly specular reflections and refractions of each light ray according to the laws of geometrical optics.

Fig. 1 exemplifies the refraction of a light ray (magenta line) through a glass sphere. The "pbrt" code was slightly modified in the present work to record the correspondences between points on an investigation plane at $z = 0$ and points on the image plane. The implementation admits non-

74

injective (i.e., non-unique) correspondences between points in the world and points on the camera sensor, since a light ray originating at the principal point can reach a point on the investigation plane that was already hit by another ray after reflections and refractions. It is important to mention that, since an image is composed of pixel elements, it has a discrete domain and, therefore, multiple light rays can also pass through the same pixel element, further increasing the multi-valuedness between mapped points. The image correction implemented here uses as pixel intensity values a weighted average of all intensities obtained by following rays through the pixel. Intensity values that correspond to light rays with fewer bounces in the scene (fewer reflections and refractions) contribute thereby, on average, more.

The present work explores configurations with the camera orthogonally positioned in relation to the investigation plane (as the example in Fig. 1). Since small rotations of the camera sensor always exist in experimental arrangements, even for precise alignments, such offsets from the perfect orthogonal setup must be taken into account. In the present implementation, slight rotations of the camera sensor in the actual experimental arrangement (optical misalignment) and lens aberrations are corrected by camera image dewarping that is used before the ray tracing mapping is applied. The dewarping is based on a 2D 2nd-order polynomial transformation (Matlab image processing toolbox). The polynomial coefficients are obtained from points on a planar target in an environment without any transparent objects in front of the camera, and their correspondent points in the computer-generated image in a similar environment. The target points must fill the entire region of the image in order to avoid incorrect distortions of the dewarped images as an artifact of the polynomial fit. The polynomial transform is applied in the acquired images with optical distortions (i.e., with transparent objects in front of the camera) and then image borders are cropped to match the field of view of computer-generated images (mapped region). Zha and coworkers successfully implemented a similar initial image pre-processing to correct for lens distortions and movements of a transparent piston in front of the camera, both not accounted for in their ray-tracing algorithm.[25]

The proposed image correction can be summarized as follows:

    1) image dewarping based on a 2nd-order polynomial transformation;

    2) image cropping to the mapped region;

    3) image correction based on ray-tracing mapping.

We selected a configuration with one sphere to present the image correction processing in Fig. 2. The configuration was composed of one 100-mm-diameter sphere in front of a 2D chessboard target with 2.5x2.5 mm grid spacing imaged by a 250-mm-distant camera equipped with a 35-mm lens. The acquired image (Fig. 2a) displays optical distortions caused by the sphere, as well as barrel aberrations in the image borders caused by the camera lens. The barrel aberration is clearly visible by the curved column of the chessboard grid on the right side in Fig. 2a.
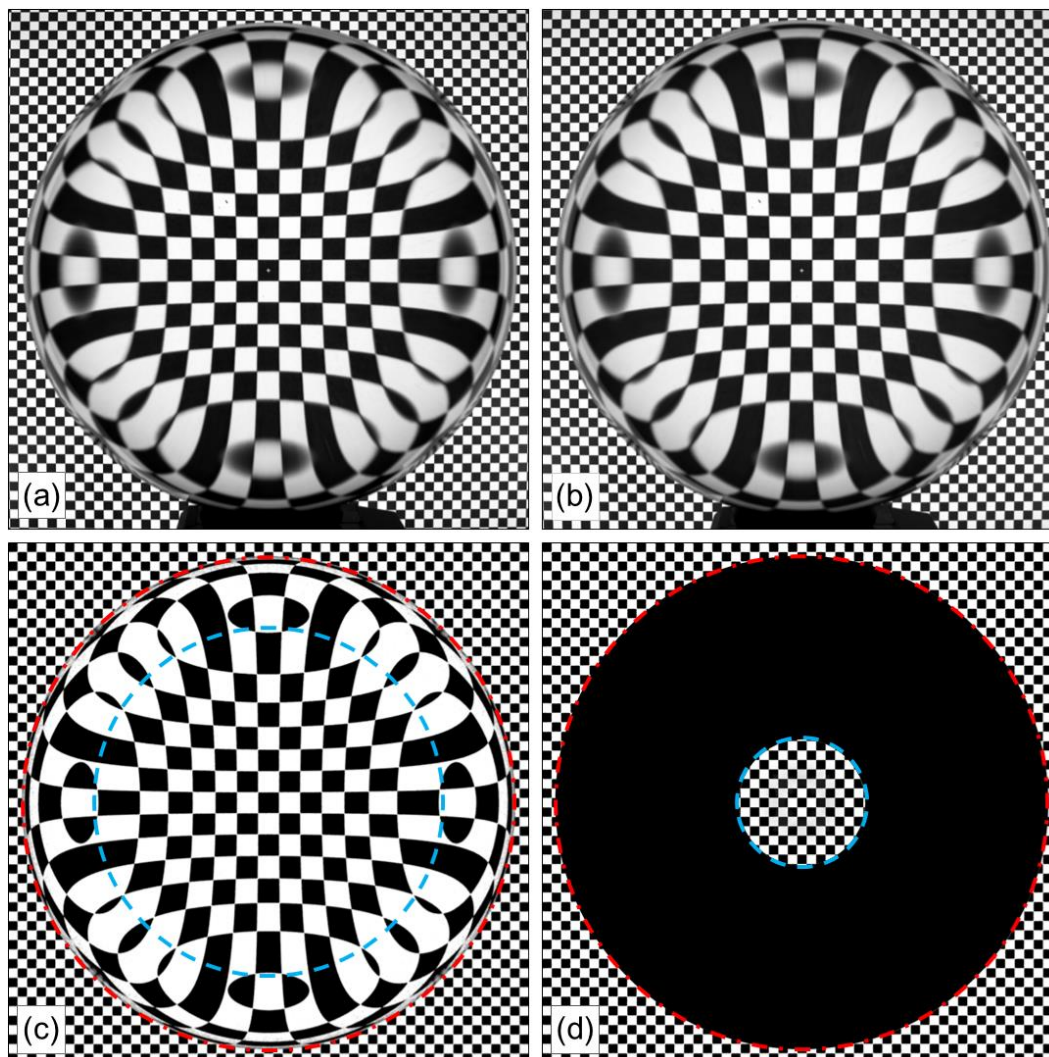
Fig. 2: Correction of high optical distortions caused by a 100-mm-diameter transparent sphere in front of a 2D chessboard target for a camera at $z = 250$ mm. (a) Acquired image, (b) image after dewarping and cropping, (c) computer-generated image and (d) corrected image based on ray tracing.

The lens aberrations were expected due to the large opening angle (sometimes also called angle of view) in combination with a short focal length. Other experimental setups of the present work did not reveal significant lens distortions as those with the 35-mm lens. The barrel-like

aberrations were mostly corrected after dewarping, as described above (Fig. 2b). The ray tracing reproduces precisely the transparent volumes in front of the camera, as can be observed by comparing Fig. 2b and Fig. 2c. The ray tracing then provides a lookup table, relating the pixel coordinate in the image plane to its corresponding point on the investigation plane. As a result, the acquired images of a target (Fig. 2a), flow or particle distribution with transparent volumes in front of the camera can be corrected to an ideal environment without transparent volumes along the camera view (Fig. 2d). Some regions close to the rim can thereby not be recovered since the optical distortion is very large. This issue will be discussed in Section 4. The non-recovered region is masked out in Fig. 2d. The boundaries of the recovered field of view in the one-sphere configuration are superimposed in Fig. 2c and Fig. 2d. Red dashed-dot circles represent the outside region, while blue dashed circles correspond to the interior region behind the sphere.

3 Experimental setups

The present work uses three test cases to analyze the influence of multiple spheres in front of the camera. Therefore, the experimental setups were slightly different among the tests.

The main experimental setup consisted of one LaVision Imager HS camera (2016x2016 pixels, pixel size of 11x11 μm, grey level of 12 bit) assembled on a 3D geared head, mounted on a two-axis linear translation stage. The camera rig was mounted on a 2-m-long rail that allowed camera displacement along its viewing direction. Transparent volumes could be precisely placed anywhere in front of the camera by means of a three-axis linear translation stage with 10 μm of precision, mounted on the same 2-m-long rail. We used clear-glass, full-material spheres as transparent volumes causing optical distortions. The spheres, bought from benfershop.de, were made of optical borosilicate crown glass. They presented excellent optical quality and dimensional precision, without imperfections on the surface or air bubbles inside.

The first test case focused on optical distortions of target images. To this end, a rigid aluminum frame, fixed on another three-axis linear translation stage with 10 μm of precision, was placed parallel to the camera lens at the end of the 2-m-long rail. A 2D chessboard target with a 2.5x2.5 mm grid printed on a transparent plastic sheet was fixed in the frame. A printed cross in the middle of the target guided the alignment of the camera and spheres. A continuous white LED panel (620x620 mm, 40 W, 4000 K) provided homogeneous back illumination of the target for camera acquisition. The apparatus allowed us to study camera calibration as well as optical distortions. The camera was set with different lenses, namely 35-mm, 60-mm and 105-mm Micro

Nikon-Nikkor lenses, according to the camera position in order to keep a field of view of about 140x140 mm.

The second test case studied the PIV evaluation for the known displacement of a printed particle field behind multiple spheres. The particle field was printed on a transparent plastic sheet from a grey intensity image generated by an in-house Matlab code. The software randomly positioned particles in the image area according to a specified particle density. The image of each particle was created considering its intensity as a 2D Gaussian with standard deviation equal to 1/4 of the particle diameter. The printed particle field was fixed in the aluminum frame. Then, the frame system emulated a particle displacement field, translating the printed particle field along the x- or y- axis (investigation plane) with a precision of 10 μm. The particle field was back-illuminated by the white LED panel during camera acquisition. Particle Image Velocimetry measurements were simulated by acquiring two images: one before and a second after translation.

The third test case analyzed actual PIV measurements of an air flow behind spheres. A vertical low-turbulent air-jet flow developed from the exit of a 5-mm-diameter pipe with its center around z = 0 and x = 0 and positioned below the investigation region. The jet flow was generated by compressed air and was adjusted by a needle valve downstream the pressure regulator. The camera was equipped with a 60-mm Micro Nikon-Nikkor lens, set with an aperture of 22 and positioned at z = 500 mm. The aluminum frame was only employed for camera calibration and then removed from the test section. A NewWave Gemini laser (2x100 mJ at 10 Hz, Nd:YAG, 532 nm) was used as a light source. Two mirrors were employed to change the laser beam direction. Spherical and cylindrical lenses shaped the laser beam coming from the left of the investigation plane to a laser sheet with a central thickness of about 1 mm. The flow was seeded by Di-Ethyl-Hexyl-Sebacat (DEHS) particle tracers of around 0.5 μm produced by an aerosol generator (ATM 225). Since no camera filter was used, the spheres were slightly offset by 4 mm from the center of the laser sheet, in order to avoid damage to the camera sensor due to possible strong reflections on the sphere surfaces. The commercial software DaVis 8 from LaVision controlled a time unit that synchronized laser firing and image capture. The software was also employed to compute the PIV fields.

Fig.3 shows a picture of this PIV setup. In this fig., a vertical air jet flows behind an aligned arrangement of three transparent 50-mm-diameter spheres and is illuminated by a green laser sheet.
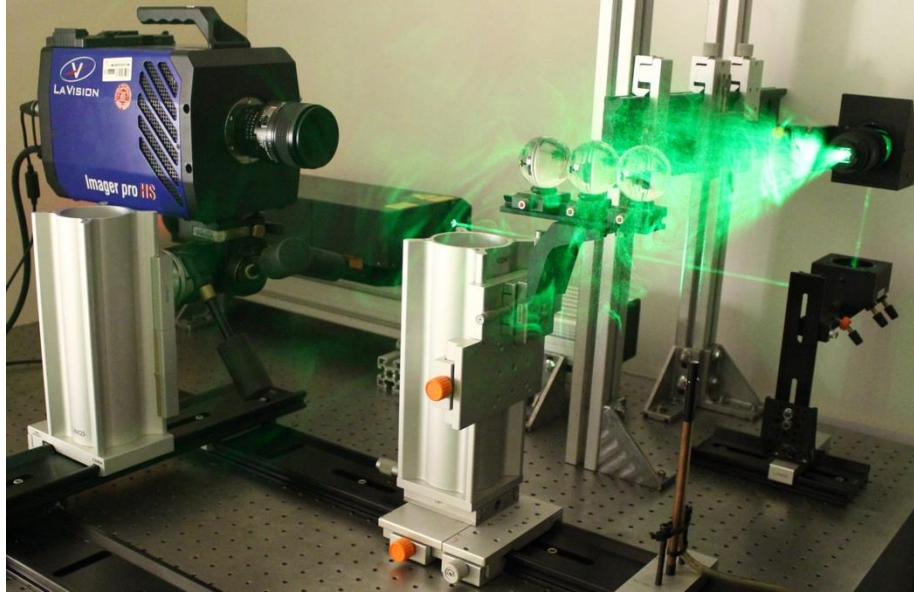
Fig. 3: Picture of the PIV experimental setup with an aligned arrangement of three transparent spheres, placed between the camera and the laser sheet.

4   Results and discussion

In the following, we discuss the influence of one and multiple spheres in front of the camera view in the three test cases: the first considers optical distortions of target images, the second the PIV evaluation of a displacement of a printed particle field, and the third PIV measurements of an air flow.

4.1   Optical distortion of target images

We start discussing the recovered field of view (FOV) and the optical distortions behind one and multiple spheres, because in practice some obstructed regions are expected after image correction. This issue is exemplified in Fig. 2d. We tested configurations composed of one sphere at two different camera positions, two and three aligned spheres touching each other with the first one in contact with the target, and a pyramidal arrangement with five spheres with each one touching at least three neighbors and a minimum distance from the target of 3 mm. The optical distortion patterns changed with the sphere dimension, number of spheres in the arrangement, their positions and the material. Fig. 4 presents computer-generated images, based on ray tracing, for the five aforementioned configurations of transparent spheres in front of a 2D chessboard target with colored markers. Different symbols were employed as markers along the southeast diagonal in the 3D virtual environment to better understand the optical distortions that

occur. The order of the target markers along the diagonal are presented in Fig. 4f, beginning with the white cross at the center of the target and ending with the green triangle at the bottom-right.

Lenses with different focal lengths f were employed to keep the overall FOV nearly constant for a given camera position L (i.e., similar image amplification). The images are cropped in order to improve readability. The computer-generated images qualitatively show mappings from the world to the camera space of these marker positions. The solid spheres work as magnifying lenses in the central region.

The one-sphere arrangement (Fig. 4a) displays a pincushion distortion in its central region. The optical pattern in the rim region of the same arrangement was a result of interior reflections of the central region behind the sphere, as observed by the mirroring effect of the southwest diagonal after the yellow triangle symbol. Therefore, no additional information could be retrieved from the rim region after the yellow triangle. Moving the camera away from the one-sphere arrangement (Fig. 4b) decreases the number of markers restored inside the sphere with the mirroring effect already starting after the pink square. Adding a second sphere along the camera viewing direction (Fig. 4c) corrected some of the optical aberrations caused by the first sphere so that almost the entire field of view behind the two spheres could be recovered, although the image was now mirrored with respect to the northeast diagonal in a barrel-like distortion. The three-sphere arrangement (Fig. 4d) yielded optical distortions similar to those caused by just one sphere, but as a mirrored image. The curvature effects were more pronounced in the three-sphere arrangement compared to that with two spheres. The external region of the rim reflected part of the target that was outside the spheres (grey triangle, orange cross and red diamond symbols), not delivering additional information behind the spheres. The five-sphere pyramidal arrangement (Fig. 4e) presented optical distortions comparable to those of the two spheres for the spheres placed on the base of the pyramid. The spheres at the base allowed the visualization of symbols from the yellow triangle to the yellow circle. The sphere at the top of the pyramid displayed a deformation similar to a 4-pointed star and recovered a region from the white cross to the red filled diamond. The pyramidal arrangement precluded observation of the region comprising the orange down-pointing triangle, grey diamond and yellow star markers, and replicated some information from the yellow triangle to the red filled diamond.
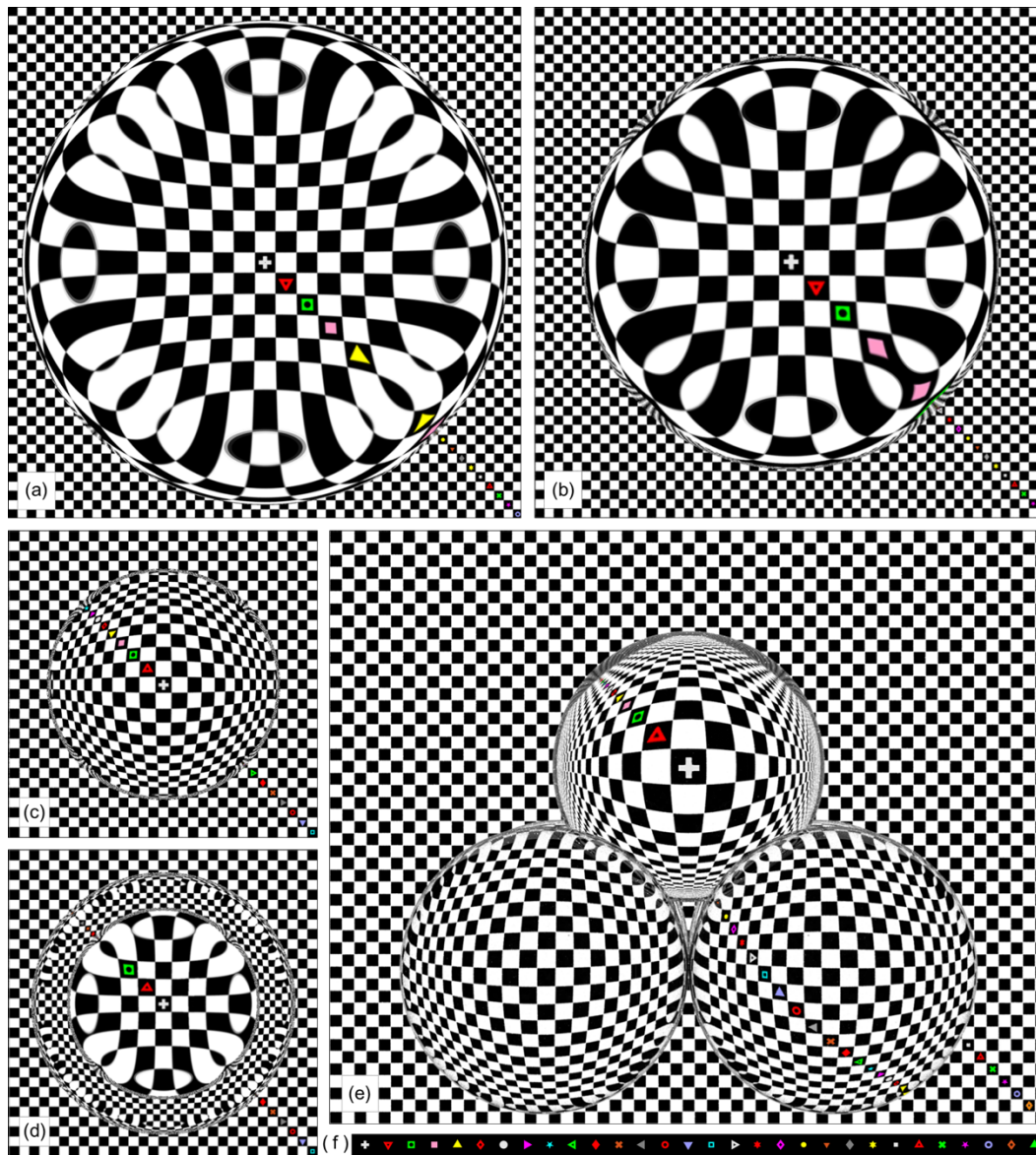
Fig. 4: Computer-generated images displaying the mapping of target markers along the southeast diagonal for different aligned arrangements of transparent solid spheres: (a) one 100-mm-diameter sphere ($L = 250$ mm, $f = 35$ mm), (b) one 100-mm-diameter sphere ($L = 500$ mm, $f = 60$ mm), (c) two 50-mm-diameter spheres ($L = 500$ mm, $f = 60$ mm), (d) three 50-mm-diameter spheres ($L = 500$ mm, $f = 60$ mm), and (e) pyramidal configuration with five 50-mm-diameter spheres ($L = 500$ mm, $f = 60$ mm). (f) The order of markers along the diagonal is presented on the bottom.

Fig. 5 quantifies the optical distortions for a variety of arrangements of spheres. Experimental setups with one, two and three aligned solid glass spheres for different camera distances are presented as symbols. Computational results using ray tracing for three configurations of borosilicate crown glass spheres ($n = 1.53$) and for one acrylic sphere ($n = 1.49$) are also plotted

as lines. A grey dashed line for the case without distortion ($n = 1.00$) is drawn for reference. In the fig., r_i is the radial distance from the sphere center to a point in the image, r_o is the radial distance in the physical space computed using the calibration target, R is the radius of the sphere, and L is the camera distance to the target. The sphere radius in the camera image is usually greater than the actual radius R, allowing relative radial positions above unity in the plots. Placing the sphere configuration in front of the target leads to magnified images of the region behind the sphere. The computational results (solid lines) adequately predict the experimental data points for well-defined volumes in front of the camera. The optical distortions do not depend on the focal length (see e.g. red square, blue down-pointing triangle and green circle) but on the camera position (see e.g. green circle, black circle and black left-pointing triangle) as observed by the experimental data (symbols in Fig. 5). For instance, the recovered central field of view for the one-sphere arrangement increased when the camera distance decreased reaching a maximum recovered region of $0 < r_o/R < 0.35$ for the cases studied. The inflection in the curve for the simulated one-sphere cases (dashed blue and solid red lines) translates the reflections observed in Fig. 4. The retrieved field of view behind the three-sphere arrangement ($0 < r_o/R < 0.37$; blue squares) was greater than that of the one-sphere arrangement for the same camera distance of $L/R = 20$ ($0 < r_o/R < 0.24$; magenta diamonds). The field of view behind two-spheres was fully restored (grey circles), displaying additionally some information of the target that was in the projected rim of the sphere arrangement greater than the sphere radius ($0 < r_o/R < 1.13$). In practice some small obstructed regions are expected at the sphere rim due to spurious reflections and the limited resolution of the digital image sensor. For the configurations with two spheres (grey circles and black solid line), the region $0 < r_o/R < 0.50$ in the physical space is amplified to $0 < r_i/R < 0.65$ in the image, while the region $0.50 < r_o/R < 1.13$ is shrunken to $0.65 < r_i/R < 1.10$. Therefore, it is anticipated that the accuracy in image restoration close to the rim will decrease with the distance from the sphere center.
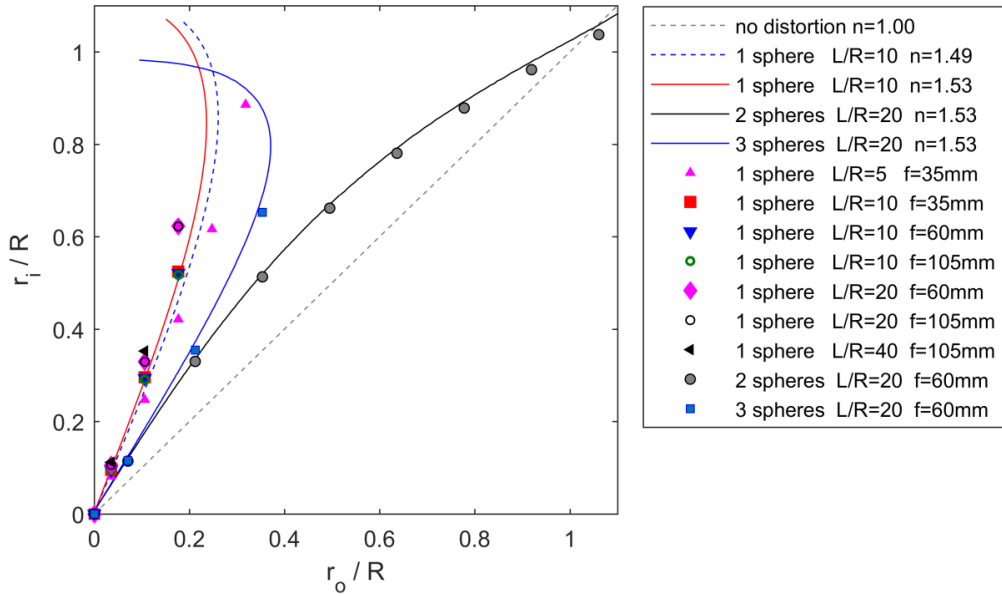
Fig. 5: Optical distortion effects in arrangements with solid spheres.

In Fig. 5, a synthetic curve of a solid sphere made of acrylic is also plotted for comparison (blue dashed line). One observes that the changes in magnification along the sphere radius are smaller than those for spheres made of borosilicate crown glass (red solid line). This means that the optical distortions increase with the refractive index. The same finding was reported by Kang and coworkers for moderate distortions caused by hemispherical lenses.[23] However, actual solid acrylic spheres seem to display less transparency and homogeneity, compared to the solid glass spheres employed in the present work. Additionally, even smaller changes in magnification are expected for hollow spheres as observed in previous work of our group.[22]

Table 1 shows a quantitative evaluation of the overall recovered field of view for experimental configurations with one, two and three aligned spheres with diameter $2R$, focal length f and camera distance to the target plane L. Two metrics are presented: (i) the restored central area in relation to the sphere cross-sectional area (a circle between red dashed-dot and blue dashed circles in Fig. 2), FOV_{in}, and (ii) the total restored area in relation to the area of a rectangle bounding the sphere projection (red dashed-dot circle in Fig. 2), FOV_{total}. The FOV_{in} increased from 3.1 % to 10.1 % shortening the distance between camera and target for the one-sphere arrangements tested. Nevertheless, the opening angle also increased when the camera distance decreased. Since there was a faster increase of the diameter of the circular limit given by the red dashed-dot line in Fig. 2 compared to the diameter of blue dashed circle, the region obstructed by the sphere rim was increased. Therefore, the FOV_{total} marginally changed from 23.7 % to 26.0 %

when the camera was translated towards the target. The FOV_{total} for a three-sphere configuration was about the same as that for one sphere. The metric FOV_{in} shows a value greater than 100 % for the two-sphere configuration. This value is expected because the change in magnification for the two-sphere arrangement allows one to recover regions not only behind but also outside the sphere (Fig. 4 and Fig. 5). The FOV_{in} for the image correction of an acquired image with two spheres is expected to be smaller due to reflections in the rim region and slight misalignment of the spheres in the actual experimental setup. The experimental arrangement that yields the best recovered field of view was that composed of two aligned spheres with a relative recovered area of 98.7 %.

Table 1: Relative recovered field of view for inside and total regions for configurations with one, two and three aligned glass spheres.

Sphere configuration				FOV_{in} (%)	FOV_{total} (%)
one sphere	$2R = 100$ mm	$L = 1000$ mm	$f = 105$ mm	3.1	23.7
one sphere	$2R = 100$ mm	$L = 500$ mm	$f = 60$ mm	4.5	24.3
one sphere	$2R = 100$ mm	$L = 250$ mm	$f = 35$ mm	10.1	26.0
two spheres	$2R = 50$ mm	$L = 500$ mm	$f = 60$ mm	>100	98.7
three spheres	$2R = 50$ mm	$L = 500$ mm	$f = 60$ mm	27.0	27.0

Fig. 6 presents the correction of optical distortions caused by two 50-mm-diameter spheres in front of a 2D chessboard target. The camera was positioned at $z = 500$ mm and set with a 60-mm lens. The acquired camera image after dewarping (Fig. 6a) is in excellent agreement with the computer-generated image (Fig. 6b). The optical aberrations in the camera image were successfully corrected, recovering almost entirely the field of view behind the spheres (Fig. 6c), as anticipated from the plot in Fig. 5.
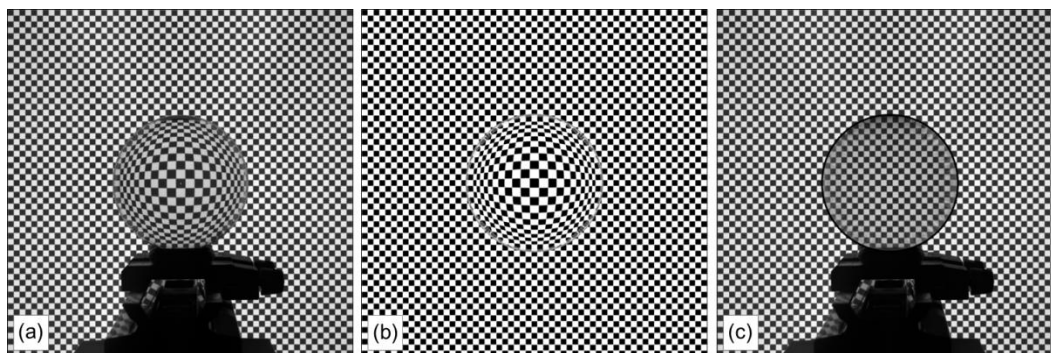
Fig. 6: Image correction of optical distortions caused by two 50-mm-diameter spheres in front of a 2D chessboard target for a camera positioned at 500 mm. (a) Acquired image after dewarping and cropping, (b) computer-generated

image based on the estimated setup parameters, and (c) corrected image.

We observed in Fig. 2 and Fig. 6 that the optical aberrations of a 2D chess-board target behind spheres can be well reconstructed by means of ray tracing using the 3D model of the experimental setup. The acquired camera images (Fig. 2a and Fig. 6a) were in excellent agreement with their corresponding computer-generated ones (Fig. 2c and Fig. 6b). Only a slight blur in the pattern inside the rim region of one-sphere arrangement (Fig. 2a) was not reproduced in the computer (Fig. 2c). The blur effect seems to be a result of chromatic aberrations, because the white illumination provides a wide range of light wavelengths and, therefore, a variation in the associated refractive indices. The present implementation of ray tracing uses a fixed refractive index ($n = 1.53$) and does not account for focal depth, producing images with sharp edges. These two aspects seemed to be of minor importance for the proposed image correction, since the central investigation region is unaffected and the laser light in the actual PIV experiment has a precisely defined light wavelength.

Table 2 summarizes the computed errors ε for one, two and three aligned spheres (last three configurations of Table 1). The errors behind the spheres are expressed as root-mean-square (*rms*) and average (*bias*) values of the differences between target points in computer-generated images and their corresponding points in the acquired images after dewarping and cropping, as well as the differences between target points in the image after correction based on ray tracing and their paired positions in a regular grid. Greater errors were observed for the three-sphere arrangement. Slight misalignment of these three spheres in the actual experiment seems to be the main reason for these error levels, because the 3D environment to generate the ray tracing mapping needs a precise model of the physical space. The error with one sphere seems to be caused by the lens nonlinearity that was not sufficiently corrected in the dewarping pre-processing. The configuration with two spheres yielded the lowest errors in the tested cases, with levels below 0.75 pixel. The error increased with radial distance from the center, because the rim region seemed to be more sensible to inaccuracies in the environment modeling that generates the ray-tracing mapping. The error quantification is important, because the errors propagate along the image processing steps and might deteriorate the accuracy and precision of velocity measurements. But the observed error values were of the same order as those found in standard PIV calibrations,[5] without optical distortions caused by transparent objects in front of the cameras. They are hence acceptable.

Table 2: Errors of target points computed between acquired and computer-generated images, and between a reference grid and the corrected image (in pixel).

| Configuration	Error in computer-generated image				Error in corrected image			
	ε_{bias}^{x}	ε_{bias}^{y}	ε_{rms}^{x}	ε_{rms}^{y}	ε_{bias}^{x}	ε_{bias}^{y}	ε_{rms}^{x}	ε_{rms}^{y}
one sphere	0.213	-0.703	0.879	0.791	-0.328	0.163	1.275	1.341
two spheres	-0.341	0.059	0.730	0.739	-0.685	-0.450	0.731	0.687
three spheres	0.457	0.379	1.637	1.202	0.472	0.430	1.220	0.859

4.2 PIV of a printed particle field

The second test case quantifies the PIV accuracy. To this end, we performed PIV for a displacement of a printed particle field behind one and multiple spheres along the camera view. Fig. 7a and Fig. 8a show the camera image of a printed particle distribution through a 100-mm-diameter sphere and through two 50-mm-diameter spheres, respectively. Similar images as those were also acquired after 14-pixel displacement of the printed particle distribution along the northeast diagonal. The images were corrected using the present ray tracing implementation. Then, 2D displacement fields were computed by means of a multi-pass sub-pixel shift cross-correlation with a final window size of 32x32 pixels with 50 % overlap applied on a pair of pre-processed particle images. Binary masks restricted velocity field calculations to recovered regions inside and outside the spheres. The computed PIV velocity fields for each corrected configuration are represented in Fig. 7b and Fig. 8b. The particle image concentrations were around 0.02 particles per pixel (*ppp*) with an average particle diameter of circa 3 pixels in the corrected images for both configurations. Some particle elongation was observed at the rim region. The magnification of corrected images with one sphere was $M = 0.16$ (equivalent to 14.8 pixels/mm), while it was 0.14 (equivalent to 12.4 pixels/mm) with two spheres. The amount of valid vectors was about 4100 and 11000, for one and two spheres, respectively.

Both vector fields of Fig. 7b and Fig. 8b were in good agreement with reference displacement fields of the printed particle distribution (14 pixels). Few vectors are missing close to the borders of the investigation region, because particle patterns left the corresponding area in the second image. The velocity computation was restricted to regions with sufficient correction after the image processing. A small non-recovered portion in the sphere rim for the two-sphere configuration can be observed in Fig. 8b, contrasting to a large region for the one-sphere arrangement in Fig. 7b. The differences on the relative recovered rim areas between the two

configurations have been already discussed earlier in the text. The large bottom regions without vectors in Fig. 8b resulted from the mechanical support of the spheres that obstructed the camera view.
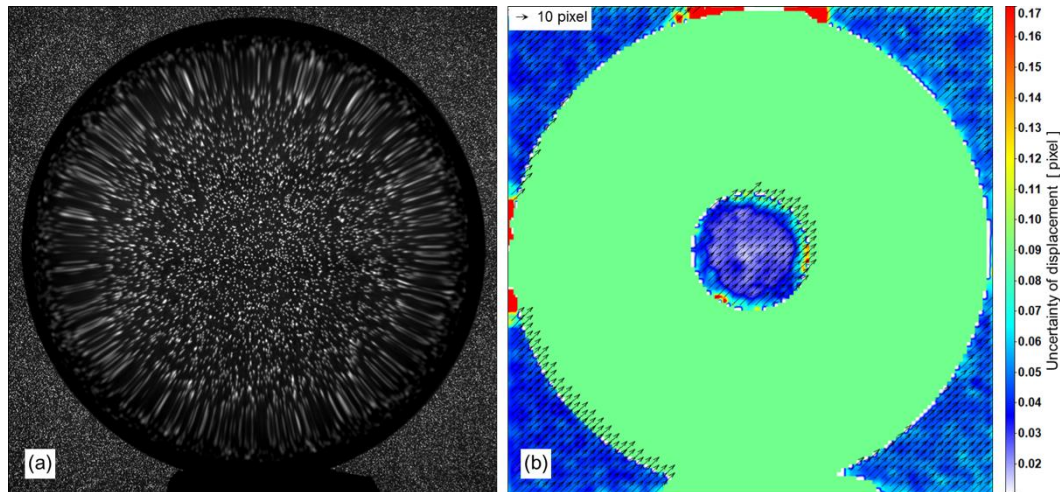
Fig. 7: (a) Acquired image of a printed particle distribution through one 100-mm-diameter sphere and (b) velocity field computed with corrected image pairs. One over two vectors are plotted for readability.
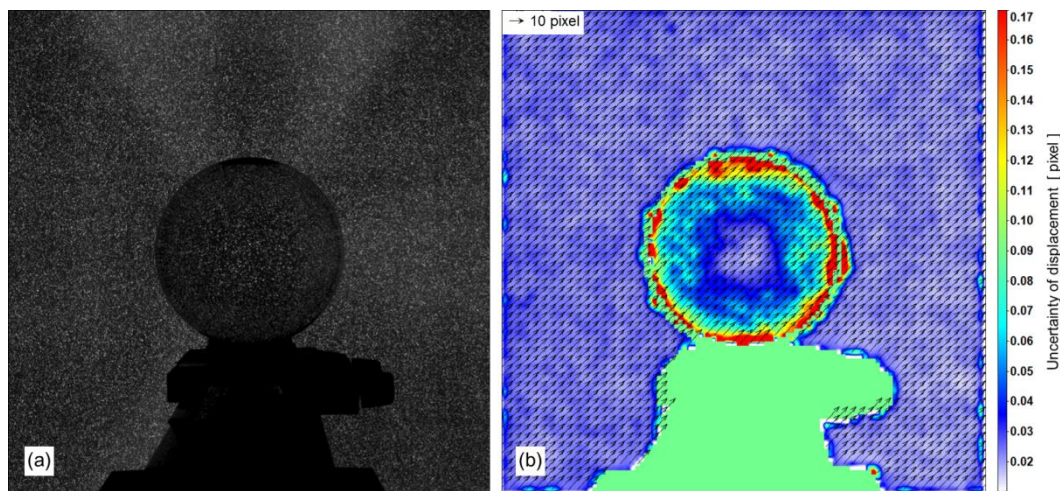
Fig. 8: (a) Acquired image of a printed particle distribution through two 50-mm-diameter spheres, and (b) velocity fields computed with corrected image pairs. One over two vectors are plotted for readability.

The standard deviation of the velocity field can be used as an estimate of the velocity errors, because no fluctuation is expected for the ideal, homogeneous displacement that was applied. The standard deviation was computed in the area behind the spheres for one vector field. The standard deviation of the velocity components in the central region behind one sphere was around 0.1 pixel, while the standard deviation of velocity in the reference field was about

0.03 pixel. The velocity fluctuation levels in the reference field accounts for a slight tilt between the printed particle plane (i.e., the aluminum frame) with respect to the expected investigation plane and the camera sensor noise, which is usually difficult to accurately reproduce in simulations. The standard deviation of the velocity in the central region for the two-sphere configuration was also about 0.1 pixel, with the standard deviation of velocity in the reference field of about 0.05 pixel. These error values are consistent with those found in the literature for accurate PIV measurements.[5]

In actual experiments, it is in general not possible to compare a velocity field with its reference field in order to compute the error and, therefore, provide the measurement accuracy, as common practice in synthetic studies. The uncertainty in the particle displacement was estimated by the Correlation Statistics (CS) Method[27] implemented in the DaVis software and is also presented in Fig. 7b and Fig. 8b as colored background. This method associates the uncertainty with the shape of the cross-correlation peak during the vector computation. The report of the uncertainty is of great importance in the measurements, because it characterizes the dispersion of values that reasonably represent the actual particle displacement (measurand). The uncertainties by CS method in Fig. 7b and Fig. 8b captured the error trend at the rim region and borders. The uncertainty levels in the sphere center were similar to those in the outside region, and the uncertainty values in the rim increased with radial distance. The overall uncertainty values slightly underestimate the actual error values (standard deviation of the velocity components) in the present work. We speculate that this difference is a result of the fact that the CS method does not account for a possible tilt between the printed particle plane and the investigation plane. Nevertheless, a further discussion about the performance of the Correlation Statistics Method in the estimation of the uncertainty is beyond the scope of this paper.

4.3 PIV of an air flow

The third test case investigated an actual PIV measurement of a vertical air-jet flow behind two configurations: a two-sphere arrangement and one with three spheres. Two and three 50-mm-diameter spheres were placed aligned with the camera viewing direction, touching each other and with the first one about 4 mm away from the center of the light sheet to minimize reflections.

The required focal depth to have the entire field of view in focus (i.e., to have the target and the sphere center sharp at the same time) changes according to the sphere configuration. The focal

depth can be estimated experimentally using a large lens aperture (equivalent to a f-number $f\# \leq 2.8$) and travelling the camera or target along the camera viewing direction. The large lens aperture leads to a small focal depth that allows for the region of interest to be scanned. The difference between extreme camera or target positions to obtain sharp images of the target at the background, rim region and center of sphere, leads to the necessary focal depth to have the entire field of view in focus. For instance, the two-sphere configuration presented in Fig. 6 required a focal depth of about 125 mm, estimated by the aforementioned methodology. These focal depths can be achieved with a small lens aperture and with the focal plane at the center of the traversed region. The focal depth δ_z is a function of the image magnification M, the f-number $f\#$ and the light wavelength λ, according to the following equation[5]:

$$\delta_z = 4.88 \left[\frac{M+1}{M}\right]^2 f\#^2 \lambda \ . \tag{1}$$

It is worth mentioning that in-focus particles are desirable to maximize PIV accuracy,[5] but a slight particle blur is acceptable, when this allows one to capture more light. Nevertheless, for some PIV experiments, especially in air flows (the application target of the present image correction), the amount captured light might be insufficient. To overcome this problem, one can increase the lens aperture to collect more light and split the field of view into two or more distinct measurement regions. For instance, one can measure the velocity field and compute statistics in the region behind the spheres with an appropriate focal plane, and afterwards measure the outside sphere region (background region or interstices of a packed bed) with another focal plane but with identical flow conditions. The joint results provide a complete picture of the flow statistics under study.

Fig. 9 presents the acquired image of a particle distribution from a seeded air-jet flow behind two transparent spheres, and its correspondent instantaneous velocity fields for a region of interest (dashed blue rectangle). The lens aperture was set to $f\# = 22$ in order to have the entire field of view in focus (Equation 1). The time delay between a pair of laser pulses and image captures was adjusted to 500 μs in order to allow a maximum displacement of around 12 pixels. The velocity field was computed in a similar way as in the previous test case (Section 4.2) except for an additional pre-processing step. The acquired images were corrected using ray tracing, then the background was subtracted by a time-minimum intensity with 4 time steps before and after the processed image, and finally the particles were normalized by a 10x10 min-max sliding-window

filter. Spurious vectors were determined by the universal outlier detection in a 5x5 window and replaced by the interpolation of valid neighbors.[5] The pre-processed images presented a magnification of 0.14, a particle concentration of around 0.03 *ppp* and an average particle diameter of about 3 pixels. As a result of the small lens aperture, the actual intensity range of the image was reduced. The maximum intensity value in the 12-bit image presented in Fig. 9a, not considering light reflections, was only 320 (with a floor noise level of 30-40 counts). The instantaneous vector fields (Fig. 9b-c) captured the main flow behavior of the jet, despite the low intensity range in the image. The average velocity field in the two-sphere configuration (Fig. 10a) was computed over 1000 realizations. Fig. 9b, Fig. 9c and Fig. 10a show the expected picture of the vertical jet flow. The optical distortions seemed to be sufficiently corrected by the ray-tracing-based image processing. In particular, the instantaneous and average velocity fields are continuous across the sphere rim and free of jumps in direction or magnitude.

We also measured the same air-jet flow behind three transparent spheres using a setup and processing analogous to those for the two-sphere arrangement. Fig. 10b shows the average velocity field in the three-sphere configuration evaluated over 100 realizations. As already discussed in Section 4.1, the recovered region behind three spheres (Fig. 10b) is much smaller than that for two spheres (Fig. 10a). Nevertheless, this case was selected in order to demonstrate that both configurations are able to deliver accurate information about the flow in the central region behind the spheres when processed by the proposed image correction. Minor differences between the average velocity fields are attributed to the different amount of realization used in the ensemble average.
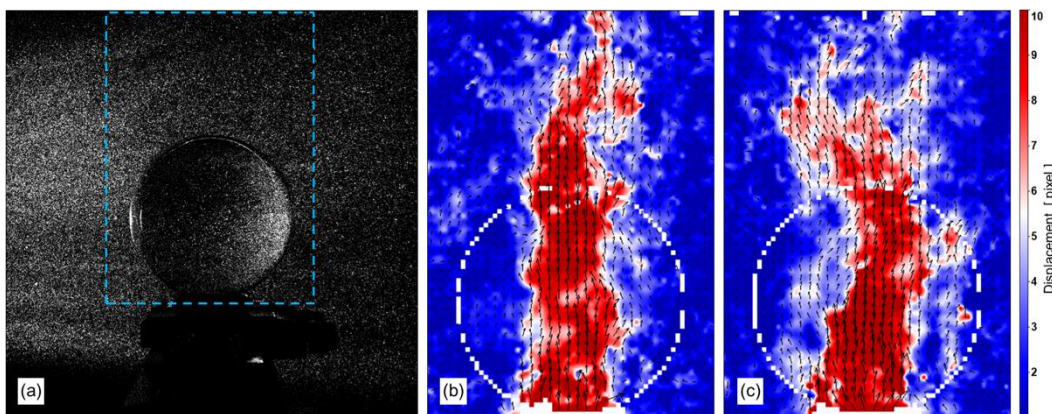
Fig. 9: (a) Acquired image of a particle distribution from an air-jet flow behind two 50-mm-diameter solid spheres, and (b-c) instantaneous velocity fields computed with an image pair after correction based on ray tracing. Color

coding corresponding to particle displacement magnitude. Only every second vector is plotted for clarity.
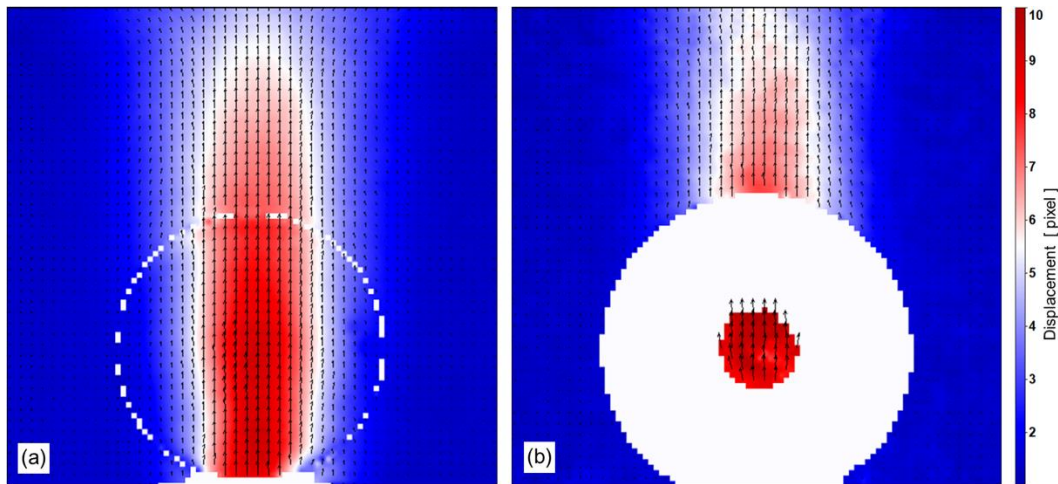
Fig. 10: (a) Average velocity field over 1000 realizations for the two-sphere configuration, and (b) average velocity field over 100 realizations for the three-sphere arrangement. Color coding corresponding to particle displacement magnitude. Only every second vector is plotted for clarity.

5   Conclusions

The present work proposes a novel image pre-processing, based on ray tracing to correct for the optical distortions caused by regular arrangements of transparent, solid spheres. Three test cases were used to study the optical aberrations caused by spheres along the camera view direction: optical distortions of target images, PIV computation of a displacement of a printed particle field, and actual PIV measurements of an air-jet flow.

Our results show that high optical distortions caused by regular arrangements of spheres can mostly be corrected using the information obtained by ray tracing a 3D computer model of the experimental setup. The recovered fields of view behind the spheres, as well as the focal depths required to image the entire investigation region were assessed for a selection of configurations. They were mainly dependent on: the sphere arrangement, the distance between the camera and the spheres, the distance between the spheres and the investigation plane, and the sphere material. The quality of the image correction was quantitatively evaluated by the computation of errors in the computer-generated images, corrected images and velocity fields. The configuration with two aligned spheres yielded the largest relative field of view and the smallest errors, which are comparable to standard PIV applications without optical distortion.

The proposed image pre-processing delivers accurate optical measurements in complex

geometries, such as air flows inside interstices of packed beds. The technique might be extended to other geometries in order to overcome limitations of the current techniques available in the field.

Acknowledgments

References

1. Blois, G.; Smith, G. S.; Best, J.; Hardy, R.; Lead, J. (2012): Quantifying the dynamics of flow within a permeable bed using time-resolved endoscopic particle imaging velocimetry (EPIV). *Experiments in Fluids*, vol. 53, no. 1, pp. 51-76.

2. Borrero-Echeverry, D.; Morrison, B. C. (2016): Aqueous ammonium thiocyanate solutions as refractive index-matching fluids with low density and viscosity. *Experiments in Fluids*, vol. 57, no. 7, pp. 123.

3. Budwig, R. (1994): Refractive index matching methods for liquid flow investigations. *Experiments in fluids*, vol. 17, no. 5, pp. 350-355.

4. Freund, H.; Zeiser, T.; Huber, F.; Klemm, E.; Brenner, G.; Durst, F.; Emig, G. (2003): Numerical simulations of single phase reacting flows in randomly packed fixed-bed reactors and experimental validation. *Chemical Engineering Science*, vol. 58, pp. 903-910.

5. Hartley, R.; Zisserman, A. (2003): Multiple view geometry in computer vision. *Cambridge University Press*, ed. 2.

6. Hassan, Y. A. (2008): Large eddy simulation in pebble bed gas cooled core reactors. *Nuclear Engineering and Design*, vol. 238, no. 3, pp. 530-537.

7. Hassan, Y. A.; Dominguez-Ontiveros, E. E. (2008): Flow visualization in a pebble bed reactor experiment using PIV and refractive index matching techniques. *Nuclear Engineering and Design*, vol. 238, no. 11, pp. 3080-3085.

8. Huang, A. Y.; Huang, M. Y.; Capart, H.; Chen, R. H. (2008): Optical measurements of pore geometry and fluid velocity in a bed of irregularly packed spheres. *Experiments in Fluids*, vol. 45, no. 2, pp. 309-321.

9. Kang, K.; Lee, S.; Lee, C.; Kang, I. (2004): Quantitative visualization of flow inside an evaporating droplet using the ray tracing method. *Measurement Science and Technology*, vol. 15, no. 6, pp. 1104.

10. Kováts, P.; Thévenin, D.; Zähringer, K. (2015): Experimental investigation of flow fields within cavities of coarse packed bed (Experimentelle Untersuchung von Strömungsfeldern in den Zwischenräumen grober Schüttungen). In *Gala, Fachtagung Lasermethoden in der Strömungsmesstechnik*, Dresden, paper 54.

11. Minor, G.; Oshkai, P.; Djilali, N. (2007): Optical distortion correction for liquid droplet visualization using the ray tracing method: further considerations. *Measurement Science and Technology*, vol. 18, no. 11, pp. L23.

12. Moroni, M.; Cushman, J. H. (2001): Statistical mechanics with three-dimensional particle tracking velocimetry experiments in the study of anomalous dispersion. II. Experiments. *Physics

of Fluids, vol. 13, no. 1, pp. 81/91.

13. Moroni, M.; Cushman, J. H.; Cenedese, A. (2009): Application of photogrammetric 3D-PTV technique to track particles in porous media. *Transport in porous media*, vol. 79, no. 1, pp. 43-65.

14. Patil, V; Liburdy, J. (2013): Flow characterization using PIV measurements in a low aspect ratio randomly packed porous bed. *Experiments in Fluids*, vol. 54, no. 4, pp. 1497.

15. Pharr, M.; Jakob, W.; Humphreys, G. (2016): Physically based rendering: From theory to implementation. *Morgan Kaufmann*, ed. 2.

16. Pokrajac, D.; Manes, C. (2009): Velocity measurements of a free-surface turbulent flow penetrating a porous medium composed of uniform-size spheres. *Transport in porous media*, vol. 78, no. 3, pp. 367.

17. Prasad, A.; Adrian, R. (1993): Stereoscopic particle image velocimetry applied to liquid flows. *Experiments in Fluids*, vol. 15, no. 1, pp. 49-60.

18. Raffel, M.; Willert, C. E.; Scarano, F.; Kähler, C. J.; Wereley, S. T.; Kompenhans, J. (2018): Particle image velocimetry: a practical guide. *Springer*, ed. 3.

19. Rong, L. W.; Zhou, Z. Y.; Yu, A. B. (2015): Lattice–Boltzmann simulation of fluid flow through packed beds of uniform ellipsoids. *Powder Technology*, vol. 285, pp. 146-156.

20. Soloff, S.; Adrian, R.; Liu, Z.-C. (1997): Distortion compensation for generalized stereoscopic particle image velocimetry. *Measurement Science and Technology*, vol. 8, no. 12, pp. 1441.

21. Tani, N.; Kondo, H.; Mori, M.; Hishida, K.; Maeda, M. (2002): Development of fiberscope PIV system by controlling diode laser illumination. *Experiments in fluids*, vol. 33, no. 6, pp. 752-758.

22. Wehinger, G. D.; Eppinger, T.; Kraume, M. (2015): Evaluating Catalytic Fixed-Bed Reactors for Dry Reforming of Methane with Detailed CFD. *Chemie Ingenieur Technik*, vol. 87, no. 6, pp. 734-745.

23. Wernet, M. P. (2000): Development of digital particle imaging velocimetry for use in turbomachinery. *Experiments in Fluids*, vol. 28, no. 2, pp. 97-115.

24. Wiederseiner, S.; Andreini, N.; Epely-Chauvin, G.; Ancey, C. (2011): Refractive-index and density matching in concentrated particle suspensions: a review. *Experiments in fluids*, vol. 50, no. 5, pp. 1183-1206.

25. Wieneke, B. (2015): PIV uncertainty quantification from correlation statistics. *Measurement Science and Technology*, vol. 26, no. 7, pp. 074002.

26. Willert, C. (1997): Stereoscopic digital particle image velocimetry for application in wind tunnel flows. Measurement science and technology, vol. 8, no. 12, pp. 1465.
Zha, K.; Busch, S.; Park, C.; Miles, P. (2016): A novel method for correction of temporally and spatially-variant optical distortion in planar particle image velocimetry. *Measurement Science and Technology*, vol. 27, no. 8, pp. 085201.